AUTOPHAGY
2024, VOL. 20, NO. 3, 629–644
https://doi.org/10.1080/15548627.2023.2277610

Taylor & Francis
Taylor & Francis Group

RESEARCH PAPER

Check for updates

Pycard deficiency inhibits microRNA maturation and prevents neointima formation by promoting chaperone-mediated autophagic degradation of AGO2/argonaute 2 in adipose tissue

Jian Li*, Hongmin Yao*, Fujie Zhao, Junqing An, Qilong Wang, Jing Mu, Zhixue Liu, Ming-Hui Zou, and Zhonglin Xie

Center of Molecular and Translational Medicine, Georgia State University, Atlanta, Georgia

ABSTRACT

PYCARD (PYD and CARD domain containing), a pivotal adaptor protein in inflammasome assembly and activation, contributes to innate immunity, and plays an essential role in the pathogenesis of atherosclerosis and restenosis. However, its roles in microRNA biogenesis remain unknown. Therefore, this study aimed to investigate the roles of PYCARD in miRNA biogenesis and neointima formation using *pycard* knockout (*pycard*$^{-/-}$) mice. Deficiency of *Pycard* reduced circulating miRNA profile and inhibited *Mir17* seed family maturation. The systemic *pycard* knockout also selectively reduced the expression of AGO2 (argonaute RISC catalytic subunit 2), an important enzyme in regulating miRNA biogenesis, by promoting chaperone-mediated autophagy (CMA)-mediated degradation of AGO2, specifically in adipose tissue. Mechanistically, *pycard* knockout increased PRMT8 (protein arginine N-methyltransferase 8) expression in adipose tissue, which enhanced AGO2 methylation, and subsequently promoted its binding to HSPA8 (heat shock protein family A (Hsp70) member 8) that targeted AGO2 for lysosome degradation through chaperone-mediated autophagy. Finally, the reduction of AGO2 and *Mir17* family expression prevented vascular injury-induced neointima formation in *Pycard*-deficient conditions. Overexpression of AGO2 or administration of mimic of *Mir106b* (a major member of the *Mir17* family) prevented *Pycard* deficiency-mediated inhibition of neointima formation in response to vascular injury. These data demonstrate that PYCARD inhibits CMA-mediated degradation of AGO2, which promotes microRNA maturation, thereby playing a critical role in regulating neointima formation in response to vascular injury independently of inflammasome activity and suggest that modulating PYCARD expression and function may represent a powerful therapeutic strategy for neointima formation.

Abbreviations: 6-AN: 6-aminonicotinamide; ACTB: actin, beta; aDMA: asymmetric dimethylarginine; AGO2: argonaute RISC catalytic subunit 2; CAL: carotid artery ligation; CALCOCO2: calcium binding and coiled-coil domain 2; CMA: chaperone-mediated autophagy; CTSB: cathepsin B; CTSD: cathepsin D; DGCR8: DGCR8 microprocessor complex subunit; DOCK2: dedicator of cyto-kinesis 2; EpiAdi: epididymal adipose tissue; HSPA8: heat shock protein family A (Hsp70) member 8; IHC: immunohistochemical; ISR: in-stent restenosis; KO: knockout; LAMP2: lysosomal-associated membrane protein 2; MAP1LC3/LC3: microtubule associated protein 1 light chain 3; miRNA: microRNA; NLRP3: NLR family pyrin domain containing 3; N/L: ammonium chloride combined with leupeptin; PRMT: protein arginine methyltransferase; PVAT: peri-vascular adipose tissues; PYCARD: PYD and CARD domain containing; sDMA: symmetric dimethylarginine; ULK1: unc-51 like kinase 1; VSMCs: vascular smooth muscle cells; WT: wild-type.

ARTICLE HISTORY
Received 29 August 2022
Revised 10 October 2023
Accepted 26 October 2023

KEYWORDS
AGO2; chaperone-mediate autophagy; miRNA maturation; neointima formation; PYCARD

Introduction

MicroRNAs (miRNAs) are endogenous small non-coding RNA molecules (containing about 21–25 nucleotides) that regulate gene expression post-transcriptionally [1,2]. Increasing studies suggest that miRNAs play a central role in vascular diseases through regulating various functions of vascular smooth muscle cells (VSMCs), such as proliferation, apoptosis, differentiation, senescence, and synthesis/secretion of extracellular matrix proteins [3,4]. MiRNAs are usually transcribed from genomes as pri-miRNAs (primary transcripts), and then processed into precursor miRNA (pre-miRNAs) and finally mature miRNAs by several proteins, including AGO2 (argonaute RISC catalytic subunit 2) [5]. AGO2 is an essential component of miRNA and small interfering (siRNA)-mediated post-transcriptional gene-silencing pathways. In mammals, AGO2 is the catalytic center of the RNA-induced silencing complex that recognizes and endonucleolytically cleaves mRNAs of complementary sequence. Although AGO2 is essential for RISC activity, the mechanisms by which AGO2 protein expression is regulated are largely unknown.

CONTACT Ming-Hui Zou mzou@gsu.edu; Zhonglin Xie zxie@gsu.edu Center for Molecular and Translational Medicine, Georgia State University, 157 Decatur Street Northeast, Atlanta, Georgia
*These authors contributed equally to this work.
Supplemental data for this article can be accessed online at https://doi.org/10.1080/15548627.2023.2277610

© 2023 Informa UK Limited, trading as Taylor & Francis Group

Autophagy is a cellular process that degrades intracellular components by lysosomes. Relative to macro- and microautophagy, chaperone-mediated autophagy (CMA) selectively degrades cytosolic proteins. This process involves binding of HSPA8 (heat shock protein family A (Hsp70) member 8) to substrate proteins *via* a KFERQ-like motif and targeting the proteins to lysosomes *via* LAMP2 (lysosomal-associated membrane protein 2). The autophagy dysfunction can lead to diseases with hyperinflammation and excessive activation of the NLRP3 (NLR family pyrin domain containing 3) inflammasome and thus acts as a major regulator of inflammasomes [6]. Since AGO2 could be degraded by CALCOCO2 (calcium binding and coiled-coil domain 2)-dependent macroautophagy [7], and AGO2 directly interacts with HSPA8 [8], we hypothesized that AGO2 might be degraded through CMA pathway.

As an important component of immune and inflammatory system, inflammasomes are crucial for host defense against infection and response to endogenous danger signals [9]. The NLRP3 inflammasome can be activated by a variety of stimuli and is implicated in chronic inflammatory and metabolic diseases. In the vasculature, activation of the NLRP3 inflammasome contributes to VSMCs phenotype switching [10–12], vascular repair, foam cell formation [13], and atherogenesis [14]. In addition, the inflammasome adaptor molecule, PYCARD (PYD and CARD domain containing) and caspase 1, are implicated in vascular inflammation, neointima formation, and atherosclerosis in mouse models. Further investigation reveals that lack of *Pycard* specifically in bone marrow cells reduces interleukin 1β and interleukin 18 expressions in neointima lesion and attenuates neointima formation after vascular injury [15]. However, emerging evidence points to the important role of PYCARD in controlling immune responses independent of inflammasome [16–18]. For example, PYCARD controls *Dock2* (dedicator of cyto-kinesis 2) expression by regulating *Dock2* mRNA stability [18]. Since RNAs could be divided into coding RNAs and noncoding RNAs (such as miRNAs), we are interested in studying whether and how PYCARD regulates miRNA biogenesis and determining whether PYCARD affects vascular injury-induced neointima formation by regulating miRNA expression.

In this study, we report that AGO2 is a CMA substrate, and discover a novel inflammasome independent role for PYCARD in controlling miRNA maturation through regulating CMA-mediated AGO2 protein degradation in adipose tissue, which contributes to vascular injury-induced neointima hyperplasia.

Results

Systemic pycard *knockout (*pycard$^{-/-}$*) mice exhibits reduced circulating miRNA profile*

To evaluate the effects of PYCARD on miRNA expression profile, we performed microarray analysis on the expression profile of 1,908 mouse miRNAs in serum samples from 8-week-old male wildtype (WT) and *pycard*$^{-/-}$ mice and found that a total of 118 miRNAs were differentially expressed (fold change > 1, or <-1) between WT and *pycard*$^{-/-}$ mice. Among them, thirty-one miRNAs were down-regulated, but no miRNA was up-regulated when threshold value was set as 1.4 (Figure 1A), because usually a threshold of $p < 0.05$ and fold change greater than 1.5-fold is applied to determine statistical significance. As demonstrated in Figure 1B, four main members of *Mir17* seed family, including *Mir17*, *Mir20a*, *Mir106b*, and *Mir93* were downregulated by 1.4 to 4.3 fold. Alignment of human miRNAs in *MIR17* and *MIR92* families showed that *MIR17* cluster contained six miRNAs (*hsa-MIR17-5p, hsa-MIR20a-5p, hsa-MIR20b-5p, hsa-MIR93-5p, hsa-MIR106a-5p, and hsa-MIR106b-5p*) that shared exact seed sequences, while *MIR92* contained three miRNA (*hsa-MIR25-3p, hsa-MIR92-3p, and hsa-MIR363-5p*) that shared same seed sequences (Fig. S1A and S1B). Consistent with the microarray finding, RT-PCR analysis showed that the expression of *Let7b*, *Let7c*, *Mir103*, *Mir17*, *Mir20a*, *Mir106b*, and *Mir93* were significantly down-regulated (Figure 1C). We also found that thirty-one miRNAs were up-regulated by 1.1 to 1.4-fold, but RT-PCR analysis of several up-regulated miRNAs, including *Mir92a*, *Mir149*, *Mir455*, and *Mir107*, did not find significant difference in these genes between WT and *pycard*$^{-/-}$ mice (Fig. S1C and S1D). Collectively, lack of *Pycard* reduces circulating miRNA expression.

Systemic pycard knockout selectively inhibits AGO2 protein expression and Mir17 seed family maturation in adipose tissue

To reveal the mechanism by which PYCARD regulates circulating miRNA expression, we detected the protein levels of key enzymes related to miRNA biogenesis in major organs that are regarded as the sources of circulating miRNA, including epididymal adipose tissue (EpiAdi), aorta, heart, liver, lung, kidney, spleen, and skeletal muscle. Compared with WT mice, *pycard*$^{-/-}$ mice exhibited a significantly lower level of AGO2, an important enzyme in regulating miRNA biogenesis, in EpiAdi, but not in other organs (Figure 2A,C). We next determined the expression of other important proteins related to miRNA biogenesis, including DICER, DROSHA, and DGCR8 (DGCR8 microprocessor complex subunit) in EpiAdi. Similar levels of these proteins were observed between WT and *pycard*$^{-/-}$ mice (Figure 2D and E). However, *Ago2* mRNA expression in WT EpiAdi was not significantly different from that in *pycard*$^{-/-}$ EpiAdi (Figure 2F), indicating that *pycard* KO post-transcriptionally regulates AGO2 protein expression, specifically in EpiAdi. We further determined the effect of *pycard* KO on AGO2 protein and *Mir17* seeding family expression in peri-vascular adipose tissues (PVAT). Similar to the finding in EpiAdi, *pycard* KO reduced AGO2 protein and *Mir17* seeding family expression in PVAT (Fig. S2A through S2C). Notably, in *pycard*$^{-/-}$ mice, AGO2 level was dramatically ($p < 0.001$) decreased in mature adipocytes, but not in stromal vascular fraction (Fig. S2D and S2E). These data indicate that mature adipocytes, but not non-adipocyte cells, are the major cells contribute to the reduction of AGO2 protein levels in *pycard*$^{-/-}$ mice.

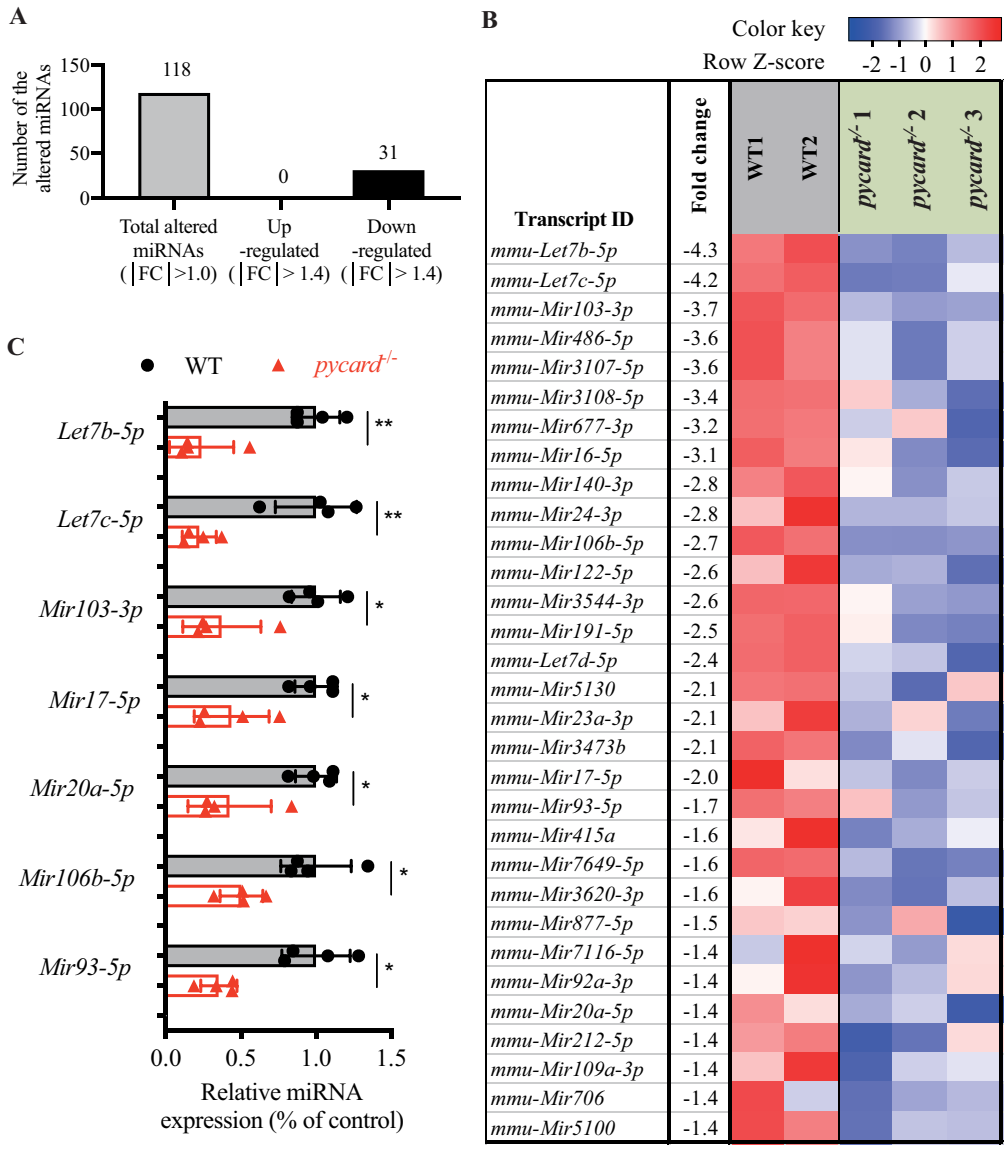

Figure 1. Systemic *pycard*$^{-/-}$ mice exhibits reduced circulating miRNA profile. (A) serum collected from 8-week-old male global *pycard*$^{-/-}$ mice and littermates (WT) were subjected to microarray analysis. Number of the altered miRnas with fold change more than 1.4. (B) differential expression of miRnas in *pycard*$^{-/-}$ mice compared with that of WT mice were shown in the table (threshold value > 1.4). (**C**) verifying the results of microarray test by RT-PCR. Data are presented as mean ± SD, n = 4 per group, * $p < 0.05$, ** $p < 0.01$ derived from Student's t tests.

To determine if lack of *Pycard* down-regulates AGO2 protein expression *via* inhibition of the NLRP3 inflammasome activity in adipocytes, we measured AGO2 protein expression after silencing other NLRP3 inflammasome components, including *Nlrp3* and *Caspase1*. The results demonstrated that silencing either *Nlrp3* or *Caspase1* did not affect AGO2 protein expression, although the NLRP3 inflammasome was inhibited as indicated by reducing cleaved caspase 1 (Fig. S2F through S2I). These results suggest that the reduction in AGO2 expression by *pycard* KO is independent of the NLRP3 inflammasome inhibition in adipocytes.

We further determined the effect of PYCARD on miRNA maturation by assessing the expression of precursor and mature *Mir17* seed family in EpiAdi of WT and *pycard*$^{-/-}$ mice. The RT-PCR results showed that 4 precursor miRNAs of *Mir17* seed family, including *Mir17-5p*, *Mir20a-5p*, *Mir106b-5p*, and *Mir93-5p* were comparable between WT and *pycard*$^{-/-}$ EpiAdi (Figure 2G). However, the mature *Mir17* seed family was significantly lower in *pycard*$^{-/-}$ EpiAdi than in WT EpiAdi (Figure 2H), indicating that *pycard* KO inhibits *Mir17* seed family maturation in EpiAdi.

AGO2 is degraded through CMA pathway

Given that AGO2 is degraded by CALCOCO2-dependent macroautophagy [7], and AGO2 directly interacts with HSPA8 [8], we reasoned that AGO2 might be degraded through CMA pathway, especially in adipocytes. To test this hypothesis, we treated the differentiated mature adipocytes with either proteasome inhibitor lactacystin, or lysosome inhibitor, NH_4Cl combined with leupeptin. The results showed that proteasome inhibition significantly enhanced protein level of runt related transcription factor 2, a well-known protein degraded by proteasomal pathway,

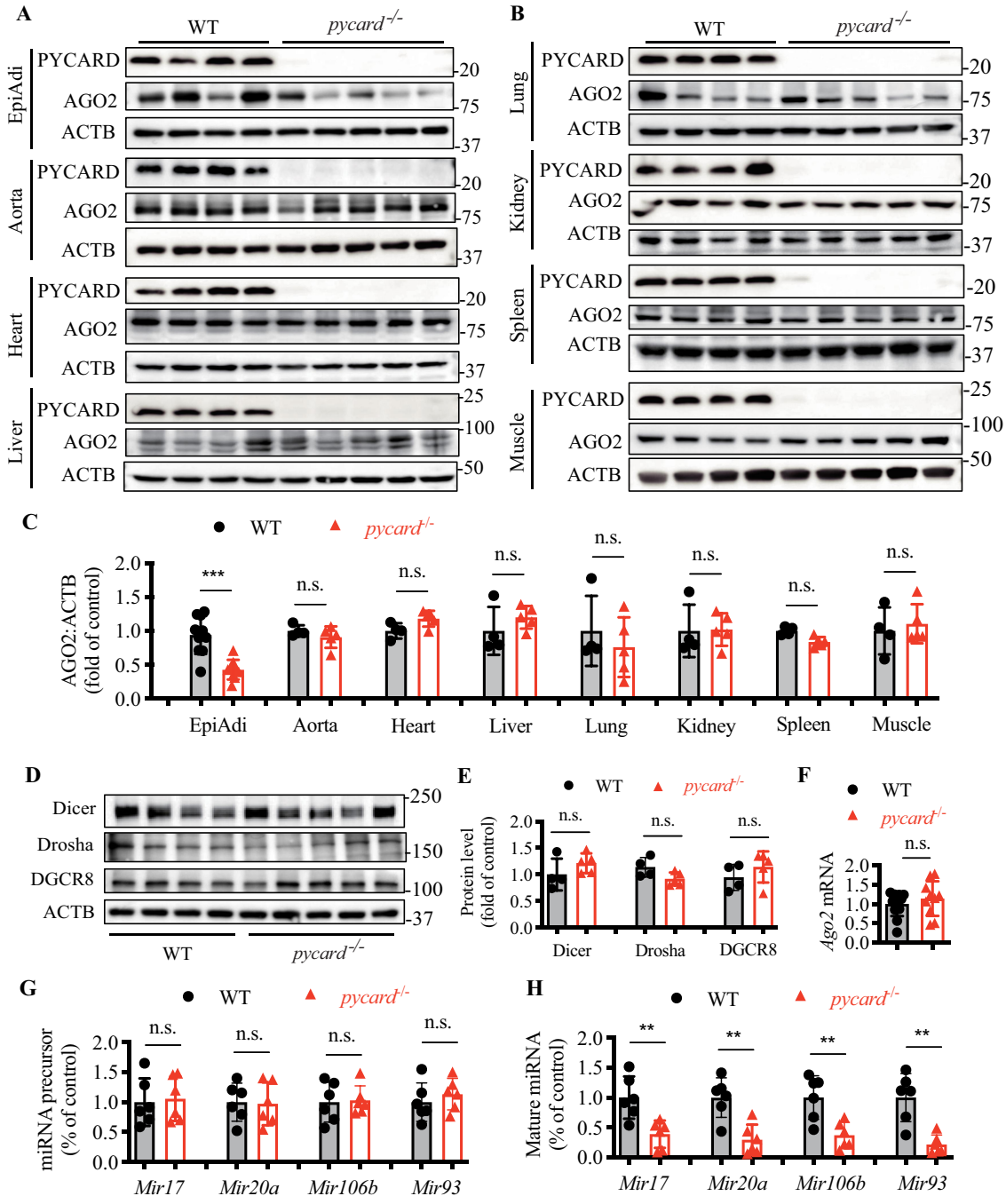

Figure 2. Systemic *pycard* KO selectively inhibits AGO2 protein expression and *Mir17* seed family maturation in adipose tissue. (A-C) immunoblotting analysis of PYCARD and AGO2 protein levels in different organs isolated from WT and *pycard*$^{-/-}$ mice. (D-E) MiRNA biogenesis-related proteins, including DICER, DROSHA and DGCR8 in epididymial adipose tissue (EpiAdi) of WT and *pycard*$^{-/-}$ mice were analyzed by western blot. (F) *Ago2* mRNA level in EpiAdi was measured by RT-PCR. (G) expressions of precursor of *Mir17* family in EpiAdi. (H) expressions of mature *Mir17* family in EpiAdi. Data are presented as mean ± SD, $n = 6$–8 per group, * $p < 0.05$, ** $p < 0.01$, and n.S. non-significant, derived from Student's t tests.

but failed to alter AGO2 protein level (Figure 3A and B). Whereas lysosomal inhibition increased the protein levels of AGO2 and myocyte enhancer factor 2D, a protein reported to be degraded by CMA pathway (Figure 3C and D), suggesting that lysosomal pathway, but not proteasomal degradation pathway, is the primary proteolytic pathway for endogenous AGO2. To verify this finding, we transfected adipocytes with either *Ctsb* (cathepsin b) siRNA (si*Ctsb*) or si*Ctsd* to inhibit lysosomal proteases activity and found that deficiency of either *Ctsb* or *Ctsd* induced AGO2 protein accumulation (Figure 3E, G). To determine whether macroautophagy is involved in AGO2 degradation, we silenced *Ulk1* (unc-51 like kinase 1), a key initiator of mammalian macroautophagy [19], and observed a significant suppression of macroautophagy, as indicted by increased SQSTM1/p62 (sequestosome 1) and reduced the ratio of MAP1LC3/LC3-II:LC3-I (Figur 3H and S3A). However, the suppression of macroautophagy by silencing *Ulk1* did not affect AGO2 protein expression (Figure 3H and I). We further determined whether CMA participates in degradation of

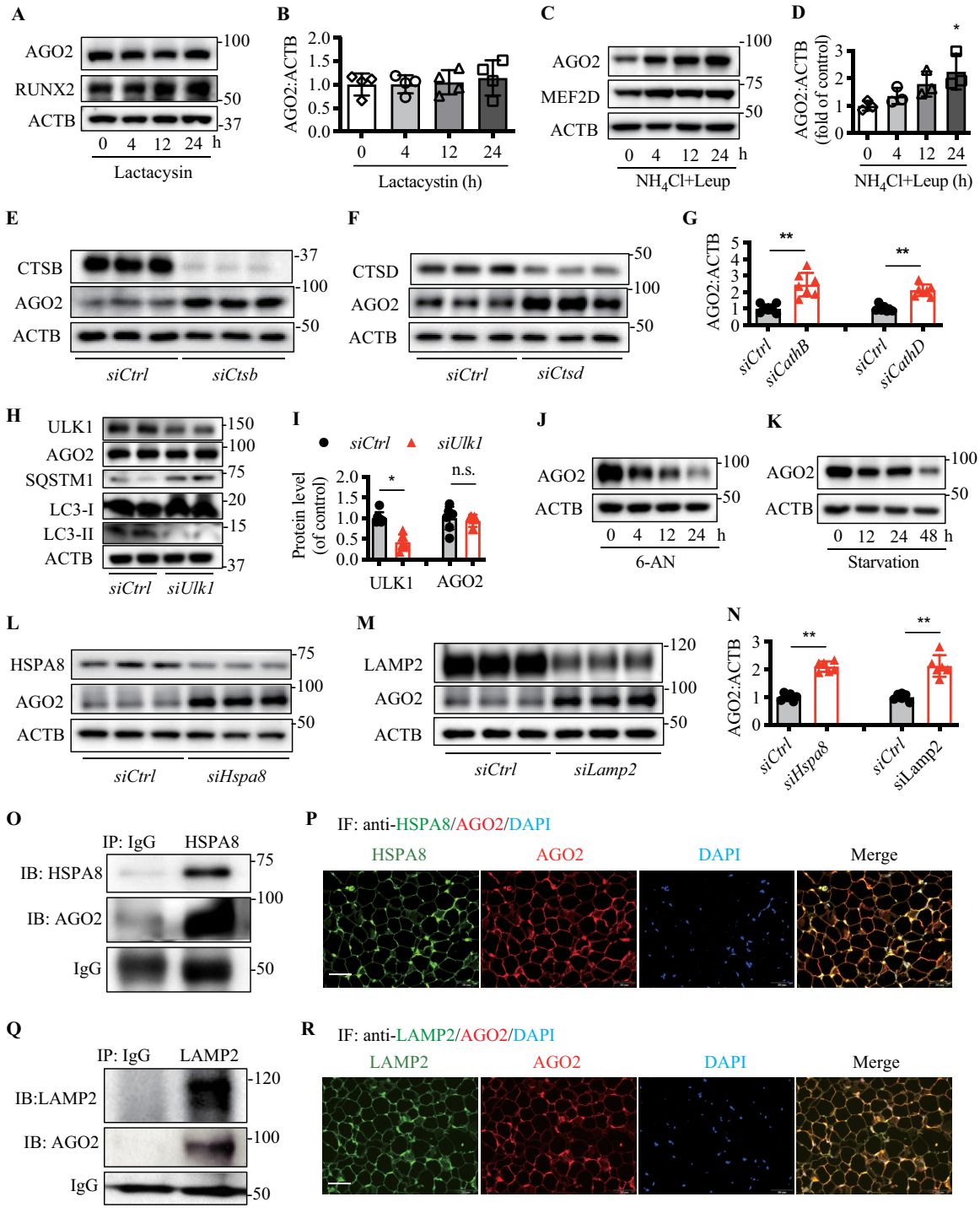

Figure 3. AGO2 is degraded through chaperone-mediated autophagy pathway. Stromal vascular fraction isolated from WT mice were differentiated into adipocytes and used for the following experiments. (A-B) immunoblotting analysis of AGO2 expression in the cells treated with 10 μM lactacystin for indicated time. (C-D) cells were treated with NH_4Cl combined with leupeptin for indicated time, and AGO2 level was measured. (E-G) cells were transfected with control siRNA (*siCtrl*) or *cathepsin B* siRNA (*siCtsb*) or *cathepsin D* siRNA (*siCtsd*), and AGO2 level was analyzed. (H-I) immunoblotting analysis of AGO2 expression in the cells transfected with control siRNA (*siCtrl*) or *Ulk1* siRNA (*siUlk1*). (J-K) cells were treated with 6-AN or starvation for indicated time, and AGO2 level was measured. (L-N) cells were transfected with control siRNA (*siCtrl*) or *Hspa8* siRNA (*siHspa8*) or *Lamp2* siRNA (*siLamp2*), and AGO2 expression was analyzed. (O) interaction of AGO2 and HSPA8 in adipose tissue were detected by immunoprecipitation and immunoblotting analysis. (P) co-staining of AGO2 and lysosomal HSPA8 in abdominal adipose tissue. Red: AGO2; green: HSPA8; blue: DAPI. (Q) the interaction of AGO2 and LAMP2 in adipose tissue was detected by immunoprecipitation and immunoblotting analysis. (R) co-staining of AGO2 and LAMP2 in abdominal adipose tissue. Red: AGO2; green: LAMP2; blue: DAPI. Data are presented as mean ± SD. * $p < 0.05$, ** $p < 0.01$, and n. S. non-significant, derived from Student's t tests.

AGO2 by using either 6-aminonicotinamide (6-AN) or long-term starvation treatment to activate CMA [20,21]. Both 6-AN treatment and starvation significantly decreased AGO2 protein level (Figure 3J, K and S3B), suggesting that AGO2 is a potential substrate of CMA. Since the CMA pathway involves two key regulators, HSPA8 and LAMP2, we used *Hspa8* siRNA and *Lamp2* siRNA to inhibit CMA and found that both siRNAs significantly increased AGO2 protein levels (Figure 3L, N). Moreover, immunoprecipitation of endogenous AGO2 in the adipocytes demonstrated that AGO2 interacted with both HSPA8 and LAMP2 (Figure 3O and Q). Consistently, immunofluorescence staining revealed that AGO2 colocalized with HSPA8 and LAMP2, the key receptor protein of CMA, in both isolated primary mouse adipocytes and 3T3-L1 adipocytes (Figure 3P, R and S3C). Finally, using the online tool KFERQ-finder (https://rshine.einsteinmed.org/) [22], we identified 5 potential KFERQ-like motifs in AGO2 protein (Fig. S3D), which may mediates lysosomal degradation of target proteins. Thus, our results support CMA as the major mode of autophagy that controls AGO2 degradation in adipocytes.

Pycard deficiency promotes AGO2 binding to HSPA8 and increases CMA-mediated AGO2 degradation in adipocytes

Next, we examined whether PYCARD affects CMA-mediated AGO2 degradation in adipocytes by treating WT and *pycard*$^{-/-}$ adipocytes with either NH_4Cl combined with Leup to inhibit lysosome activity or silencing *ULK1* to suppress macroautophagy. The *pycard*$^{-/-}$ adipocytes exhibited significantly lower AGO2 protein level relative to WT adipocytes. Administration of NH_4Cl plus leupeptin led to AGO2

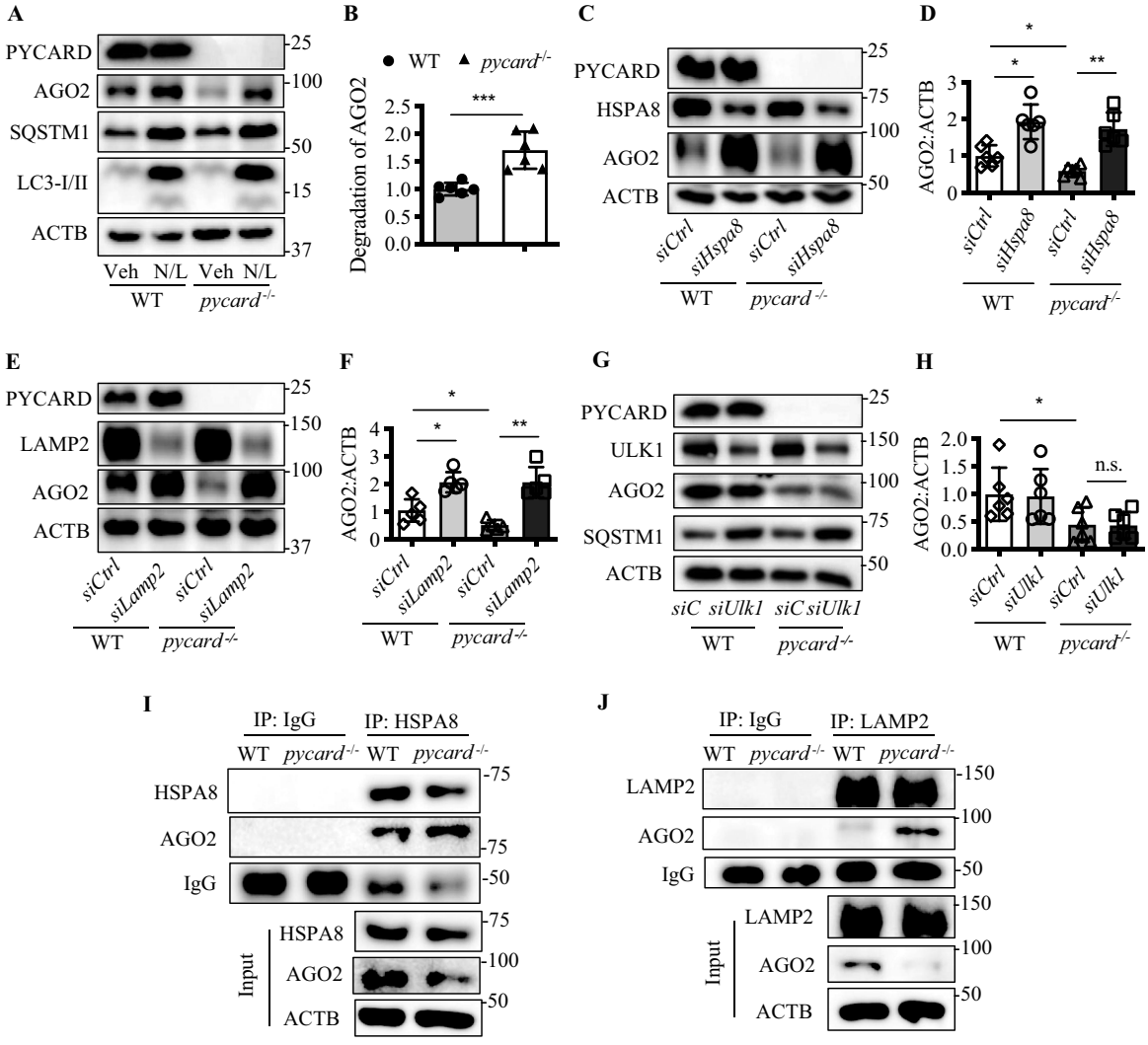

Figure 4. *Pycard* deficiency promotes CMA-mediated AGO2 degradation in adipocytes. Stromal vascular fraction isolated from WT and *pycard*$^{-/-}$ mice were differentiated into adipocytes and used for the following experiments. (A-B) cells were treated with NH_4Cl (N) combined with leupeptin (L) for 24 h. AGO2 level was detected by immunoblotting analysis. The ratio of N/L to veh treatment after normalization by endogenous control. (C-D) cells were transfected with control siRNA (*siCtrl*) or *Hspa8* siRNA (*siHspa8*), AGO2 protein level was measured by immunoblotting analysis. (E-F) cells were transfected with control siRNA (*siCtrl*) or *Lamp2* siRNA (*siLamp2*), and western blot was performed to measure AGO2 protein expression. (G-H) cells were transfected with control siRNA (*siCtrl*) or *Ulk1* siRNA (*siUlk1*), andAGO2 protein expression was analyzed by immunoblotting analysis. (I) the interaction of AGO2 and HSPA8 in differentiated adipocytes was determined by immunoprecipitation and immunoblotting analysis. (J) the interaction of AGO2 and LAMP2 was analyzed in differentiated adipocytes. Data are presented as mean ± SD. * $p < 0.05$, ** $p < 0.01$, and n.S. non-significant, derived from Student's t tests.

accumulation in WT adipocytes and prevented the reduction in AGO2 protein level in *pycard*$^{-/-}$ adipocytes, as indicated by comparable AGO2 protein levels between NH_4Cl plus leupeptin-treated WT and *pycard*$^{-/-}$ adipocytes (Figure 4A and B). Consistently, suppression of CMA by silencing either *Hspa8* or *Lamp2* increased AGO2 protein level in WT adipocytes and prevented the reduction of AGO2 protein expression in *pycard*$^{-/-}$ adipocytes (Figure 4C, F). To determine if *pycard* KO affects AGO2 degradation, adipocytes isolated from WT and *pycard*$^{-/-}$ mice were transfected with control siRNA (siCtrl) or *Lamp2* siRNA (si*Lamp2*) in the presence or absence of NH_4Cl (N) combined with leupeptin (L) (N/L). In the adipocytes transfected with siCtrl, *pycard* KO increased AGO2 degradation, and the increased AGO2 protein degradation was prevented by silencing *Lamp2* (Fig. S4A and S4B). However, inhibition of macroautophagy by silencing *Ulk1* did not prevent the decrease in AGO2 protein level in *pycard*$^{-/-}$ adipocytes (Figure 4G and H).

CMA is mediated by HSPA8 recognition of the KFERQ peptide motif in target proteins, and LAMP2 is responsible for substrate binding and internalization to lysosomes. To determine the mechanisms for PYCARD inhibiting CMA, we first examined if PYCARD regulates HSPA8 and LAMP2 protein expression. The western analysis showed that lack of *Pycard* did not affect protein expression of either HSPA8 or LAMP2, because comparable protein levels of HSPA8 and LAMP2 were observed in WT and *pycard*$^{-/-}$ adipocytes (Fig. S4C and S4D). We further examined whether lack of *Pycard* influences AGO2 binding to either HSPA8 or LAMP2. The results showed that AGO2 bound to both HSPA8 and LAMP2 in WT adipocytes, and the bindings were further increased in *pycard*$^{-/-}$ adipocytes (Figure 4I, J S4E, and S4F). Taken together, *Pycard* deficiency promotes the binding between AGO2 and CMA effectors (HSPA8 and LAMP2), increasing AGO2 degradation in adipocytes.

Increased PRMT8-mediated AGO2 methylation interrupts the association between AGO2 and HSPA8, and inhibits CMA-mediated degradation of AGO2 in pycard-deficient condition

KFERQ-like motif provides the necessary binding region to identify HSPA8 as the cytosolic chaperone that target proteins for lysosomal degradation [23]. Post-translational modifications of proteins containing the KFERQ-like motif, such as acetylation and methylation, may enable or disrupt HSPA8 binding to substrate proteins through the KFERQ-like motif [24,25]. Thus, we investigated whether post-translational modifications affect the interaction between AGO2 and HSPA8, as well as CMA-mediated AGO2 degradation in *Pycard*-deficient conditions. We first assessed the acetylated AGO2 protein expression in WT and *pycard*$^{-/-}$ adipocytes. The cells were treated with NH_4Cl combined leupeptin to inhibit lysosomal activity, and acetylated AGO2 protein was examined by immunoprecipitating with anti-acetyl lysine (Ac-lysine) antibody followed by immunoblotting with an antibody against AGO2. As shown in Figure 5A, comparable levels of acetylated AGO2 were detected between WT and *pycard*$^{-/-}$ adipocytes, indicating that *pycard* KO did not affect AGO2 acetylation in adipocytes.

Dual regulation of *Arabidopsis* AGO2 by arginine (R) methylation has been reported in plants [26]. As arginine is a key residue that constitutes the KFERQ-like motif, we examined whether PYCARD affects AGO2 methylation in adipocytes. We first determined the effects of PYCARD on protein methylation in WT and *pycard*$^{-/-}$ adipocytes using antibodies against either dimethyl-arginine, symmetric (SYM10) or dimethyl-arginine, asymmetric (ASYM24), that specifically recognize symmetric dimethylarginine (sDMA) and asymmetric dimethylarginine (aDMA) modifications, respectively. The immunoblotting analysis of total sDMA and aDMA levels in EpiAdi showed that ASYM24 level in *pycard*$^{-/-}$ adipocytes was higher than that in WT adipocytes, but the level of SYM10 was comparable between WT and *pycard*$^{-/-}$ adipocytes (Fig. S5A and S5B), indicating that *Pycard* deficiency promotes protein aDMA modification without affecting sDMA modification.

We then determined whether PYCARD affects AGO2 methylation using immunoprecipitation and western blot. Both sDMA and aDMA could be detected in the AGO2 protein pulled down from WT adipocytes (Figure 5B and S5C). Notably, similar levels of SYM10 and significantly higher levels of ASYM24 were observed in the AGO2 protein pulled down from *pycard*$^{-/-}$ adipocytes (Figure 5B and S5C), suggesting that *pycard* KO increases aDMA modification of AGO2.

ADMA is catalyzed by type I PRMT (protein arginine N-methyltransferase) proteins, including PRMT1, PRMT3, PRMT4, PRMT6 and PRMT8, while sDMA is catalyzed by type II PRMTs, which include PRMT5 and PRMT7 [27]. To identify which PRMT mediates AGO2 methylation, we assessed *Prmt1* to *Prmt8* mRNA expression in WT and *pycard*$^{-/-}$ adipocytes using quantitative RT-PCR. The results showed that only *Prmt8* mRNA was significantly increased in *pycard*$^{-/-}$ cells (Figure 5C). Consistently, western blot analysis of PRMT8 expression in *pycard*$^{-/-}$ EpiAdi and PVAT confirmed that PRMT8 expression was significantly enhanced in *Pycard*-deficient tissues (Figure 5D and S5D). Moreover, application of *Prmt8* siRNA dramatically blocked AGO2 degradation in *pycard*$^{-/-}$ cells (Figure 5E and S5E), suggesting that PRMT8 is involved in PYCARD-mediated AGO2 degradation.

We next evaluated whether PRMT8-mediated AGO2 methylation affects CMA-dependent AGO2 degradation by inhibiting PRMT8. To select a PRMT8 inhibitor for our experiments, we determined the EC50s of 4 commercially available PRMT inhibitors, including GSK3368715 (GSK), MS023, TC-E 5003 (TC-E), and EPZ020411 (EPZ). As demonstrated in Table S1, GSK3368715 and MS023 were the most potent inhibitors of PRMT8 with IC50 of 1.7 nM and 5 nM, respectively, which have more than 10-fold selectivity for PRMT8 over PRMT3 and PRMT4, although their IC50s on PRMT1 and PRMT6 were close to those on PRMT8. We further determined the effects of GSK3368715 and MS023 on AGO2 protein expression using TC-E 5003 (PRMT1 selective inhibitor) and EPZ020411 (PRMT6 selective inhibitor) as control chemicals. The western blot analysis showed that

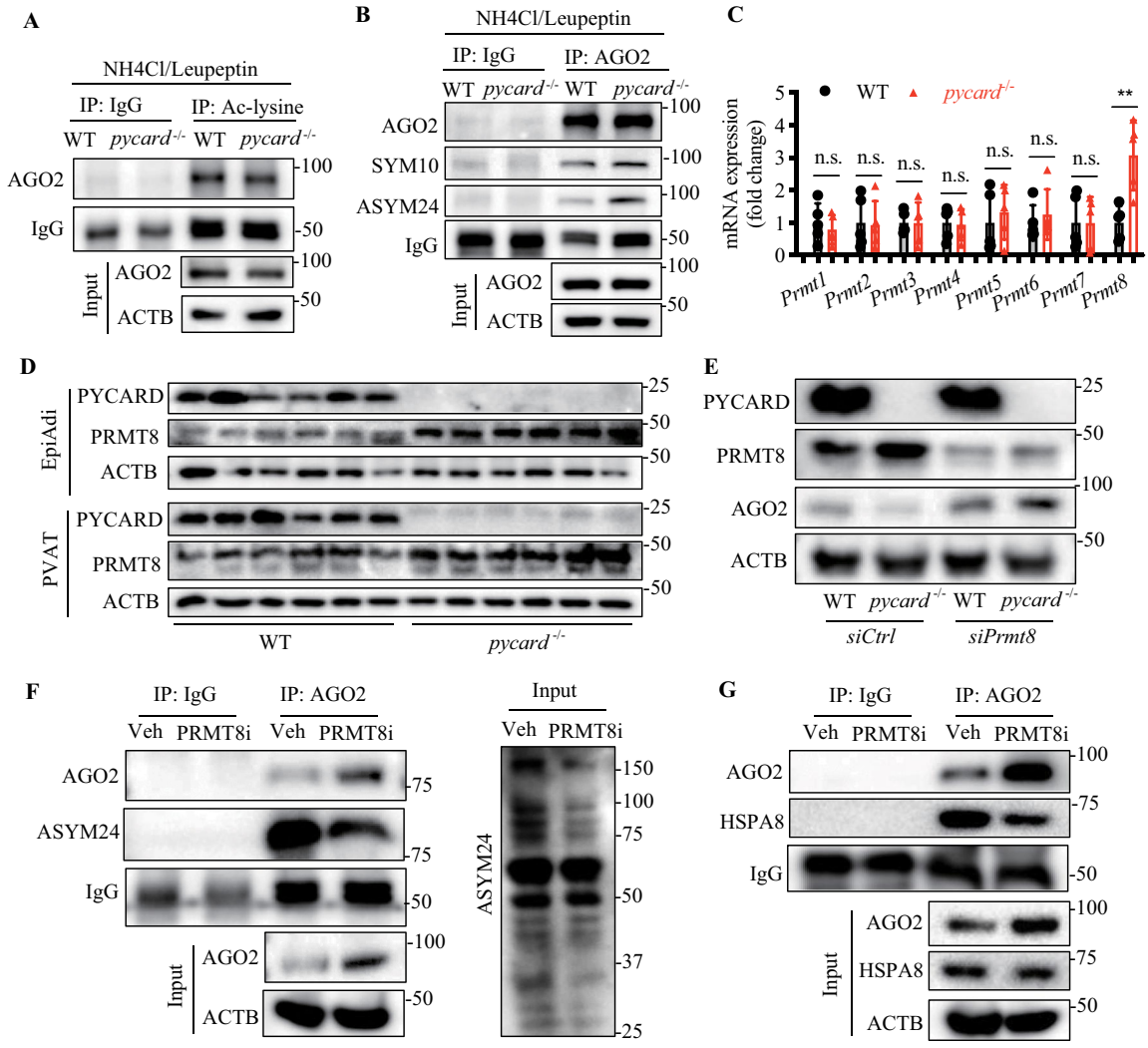

Figure 5. *Pycard* deficiency promotes PRMT8-mediated AGO2 methylation and increases AGO2 binding to HSPA8. (A) the differentiated WT and *pycard*$^{-/-}$ adipocytes were treated with NH_4Cl combined with leupeptin for 24 h. Acetylated AGO2 level was determined by immunoprecipitation (IP) of acetylate lysin (ac-lysin) and followed by immunoblotting analysis of AGO2. (B) the differentiated WT and *pycard*$^{-/-}$ adipocytes were treated with NH_4Cl combined with leupeptin for 24 h. Methylated AGO2 level was determined by IP of AGO2 and followed by immunoblotting analysis of either SYM10 or ASYM24. (C) Messenger RNA levels of PRMTs in the differentiated WT and *pycard*$^{-/-}$ adipocytes were analyzed by qRT-PCR. ** $p < 0.01$. (D) immunoblotting analysis of PRMT8 in epididymal adipose tissue (EpiAdi) or perivascular adipose tissue (PVAT) collected from WT or *pycard*$^{-/-}$ mice. (E) the differentiated WT or *pycard*$^{-/-}$ adipocytes were transfected with control siRNA (siCtrl) or *Prmt8* siRNA (*siPrmt8*), protein levels of AGO2 and PRMT8 were detected by immunoblotting analysis. (F) primary mature adipocytes were treated with PRMT8 inhibitor (PRMT8i, GSK3368715, 2 nM) or vehicle (veh) for 48 h. AGO2 methylation level was determined by IP and immunoblotting analysis. (G) primary mature adipocytes were treated with PRMT8 inhibitor (PRMT8i, GSK3368715, 2 nM) or vehicle (veh) for 48 h. The interaction between AGO2 and HSPA8 was determined by IP and immunoblotting analysis. Data are presented as mean ± SD. * $p < 0.05$, ** $p < 0.01$, and n.S. non-significant, derived from Student's t tests.

GSK3368715 and MS023 significantly increased AGO2 protein level. However, neither TC-E 5003 nor EPZ020411 affected AGO2 expression (Fig. S5F and S5G). We also examined if inhibition of PRMT8 by GSK3368715 affects AGO2 protein degradation, as shown in Figure S5H and S5I, GSK3368715 treatment significantly suppressed AGO2 protein degradation. Thus, we used GSK3368715 as a PRMT8 inhibitor in our study. In the presence of GSK3368715, aDMA modification of AGO2 was markedly suppressed (Figure 5F and S5J), meanwhile, AGO2 binding to HSPA8 was dramatically inhibited as well (Figure 5G and S5K). These data suggest that inhibition of PRMT8 prevents aDAM modification of AGO2, disrupts the association between AGO2 and HSPA8, and thus inhibiting CMA-mediated degradation of AGO2. To determine whether *pycard* KO affects PRMT8 expression in vasculature, we assessed PRMT8 expression in aortic sections and found that loss of *Pycard* significantly increased PRMT8 protein level in PVAT but had no effect on PRMT8 expression in aortas.

PRMT8 has recently been identified as a brain specific PRMT in human tissues [28]. To determine the expression pattern of PRMT8 in mouse tissues, we analyzed PRMT8 protein expression in mouse tissues, including EpiAdi, subcutaneous adipose tissue, brown adipose tissue, liver, heart, spleen, lung, kidney, muscle, brain (frontal lobe, parietal lobe, and temporal lobe), aorta, and PVAT. The result showed that PRMT8 protein was expressed not only in brain but also in some other tissues, including EpiAdi, subcutaneous adipose tissue, liver, and heart. Notably, it was also highly expressed in brown adipose tissue and PVAT (Fig. S6A and S6B). We further determined the effect of *pycard* KO on PRMT8 expression in PVAT and

aorta using immunohistochemical (IHC) staining analysis. The result showed that PRMT8 was only detected in PVAT but not in aortas, and its expression in PVAT was significantly increased in *pycard*$^{-/-}$ mice (Fig. S6C and S6D). Taken together, PRMT8 is expressed not only in brain but also in PVAT in mice. To establish clinical relevance, we examined PRMT8 protein expression in human femoral tissues. As shown in Fig. S6E, PRMT8 was highly expressed in adipose tissue compartment rather than in the small arteries of human femoral tissue.

Deficiency of pycard attenuates neointima formation in response to vascular injury

Given that the PYCARD-dependent inflammasomes are associated with vascular injury-induced neointima formation [15,29,30], and that lack of *Pycard* reduced AGO2 protein level, subsequently inhibiting the maturation of *Mir17* family *(Mir17, Mir20a, Mir106b, and Mir93)* that functionally cooperate to fine-tune signaling and developmental pathways in carotid artery restenosis [31,32], we reasoned that the PYCARD-AGO2-*Mir17* family axis might be involved in neointima hyperplasia induced by vascular injury. To test this, we performed sham or carotid artery ligation (CAL) surgery on WT and *pycard*$^{-/-}$ mice and analyzed neointima formation 4 weeks after surgery. *Pycard* deficiency did not visibly alter vessel structure. After injury, the ration of lumen to media and neointima length were significantly decreased in WT mice (Figure 6A, D), indicating increased neointima formation. Whereas *pycard* KO significantly ($p < 0.01$) prevented ligation-enhanced neointima formation.

To determine if PVAT-derived AGO2-miRNAs are involved in inhibition of neointima formation in *Pycard*-deficient conditions, we first detected AGO2 protein levels in both aorta and PVAT using western blot. The result clearly showed that *pycard* KO significantly enhanced AGO2 protein expression in PVAT but not in aorta. Even loading sample was increased by two fold, AGO2 was barely detected in aorta (Fig. S7A). The dynamic analysis of AGO2 expression in WT mice showed that AGO2 expression was significantly increased one week after vascular injury and remained at a higher level throughout the study period (Fig. S7B and S7C). The increase in AGO2 expression was accompanied by more neointima formation, as indicated by increased neointima length and the ration of lumen to media (Fig. S7D), which suggests a positive correlation between neointima formation and AGO2 expression (Fig. S7E). Notably, vascular injury-enhanced AGO2 expression in media and neointima was significantly attenuated in *pycard*$^{-/-}$ mice (Figure 6E, F). Unexpectedly, erythrocytes were also positively stained, (Fig. S7B and S7C). To test whether *Pycard* affects erythrocyte AGO2 expression, we isolated erythrocytes from WT and *pycard*$^{-/-}$ mice. As shown in the Fig. S7F and S7G, AGO2 protein level in erythrocyte was similar between WT and *pycard*$^{-/-}$ mice, suggesting that erythrocyte AGO2 May not contribute to the miRNA alteration in *pycard*$^{-/-}$ mice.

In addition, in WT mice serum *Mir106b* level was significantly increased one week after vascular injury and then gradually declined to basal level 4 weeks after the surgery (Figure 6G). Further, one week after surgery, in mice that underwent sham operation, *Mir17* family levels were significantly lower in WT mice than those in *pycard*$^{-/-}$ mice. CAL significantly increased *Mir17* family levels, and the increases were abolished in *pycard*$^{-/-}$ mice. (Figure 6H). Collectively, inhibition of the PYCARD-AGO2-*Mir17* family axis is critical for suppression of neointima formation in *pycard*$^{-/-}$ mice.

Overexpression of AGO2 or administration of Mir106b *mimic prevents pycard deficiency-mediated inhibition of neointima formation in response to vascular injury*

Since vascular injury-enhanced levels of AGO2 and circulating *Mir17* family were attenuated in *pycard*$^{-/-}$ mice, we investigated whether overexpression of AGO2 or administration of mimic of *Mir106b* (a major member of *Mir17* family) promotes neointima formation in *Pycard*-deficient conditions. To this end, we locally overexpressed recombinant His-tagged AGO2 (His-AGO2) protein or vehicle in the injured carotid artery immediately after surgery. IHC staining revealed that deficiency of *Pycard* reduced AGO2 expression, and overexpression of His-AGO2 significantly increased AGO2 level in both WT and *pycard*$^{-/-}$ mice (Fig. S8A and S8B). Lack of *Pycard* significantly inhibited vascular injury-induced neointima formation in mice transfected with vehicle. The attenuation of neointima formation in *pycard*$^{-/-}$ *mice* was prevented by overexpressing His-AGO2 protein (Figure 7A, C).

To determine whether the downregulation of *Mir17* family is involved in inhibition of neointima formation under *Pycard*-deficient conditions, we locally delivered a mimic of *Mir106b* to the injured carotid artery. After 3 days of treatment, application of *Mir106b* mimic increased serum *Mir106b* by 3 fold in both WT and *pycard*$^{-/-}$ mice and prevented the decreased *Mir106b* levels in *pycard*$^{-/-}$ mice. (Fig. S8C) To determine if the circulating miRNA expression in vasculature, we collected carotid arteries and measured *Mir106b* level in carotid arteries after 7 days of treatment. As depicted in Fig. S8D, application of *Mir106b* mimic significantly enhanced *Mir106b* in both WT and *pycard*$^{-/-}$ mouse aortas and attenuated the decreased *Mir106b* in *pycard*$^{-/-}$ mouse aortas, suggesting that the circulating miRNAs end up in the vasculature. Similar to the effect of His-AGO2 overexpression on neointima formation, *Mir106b* mimic overexpression also partially blocked the protective effect of *pycard* KO on neointima formation (Figure 7D, F). Taken together, these data indicate that activation of the AGO2-*Mir106b* pathway prevents the attenuation of neointima formation in *Pycard*-deficient conditions.

Discussion

PYCARD has been regarded as a simple adaptor protein that recruits pro-caspase-1 into inflammasomes [33]. However, emerging evidence indicates that it also plays inflammasome-

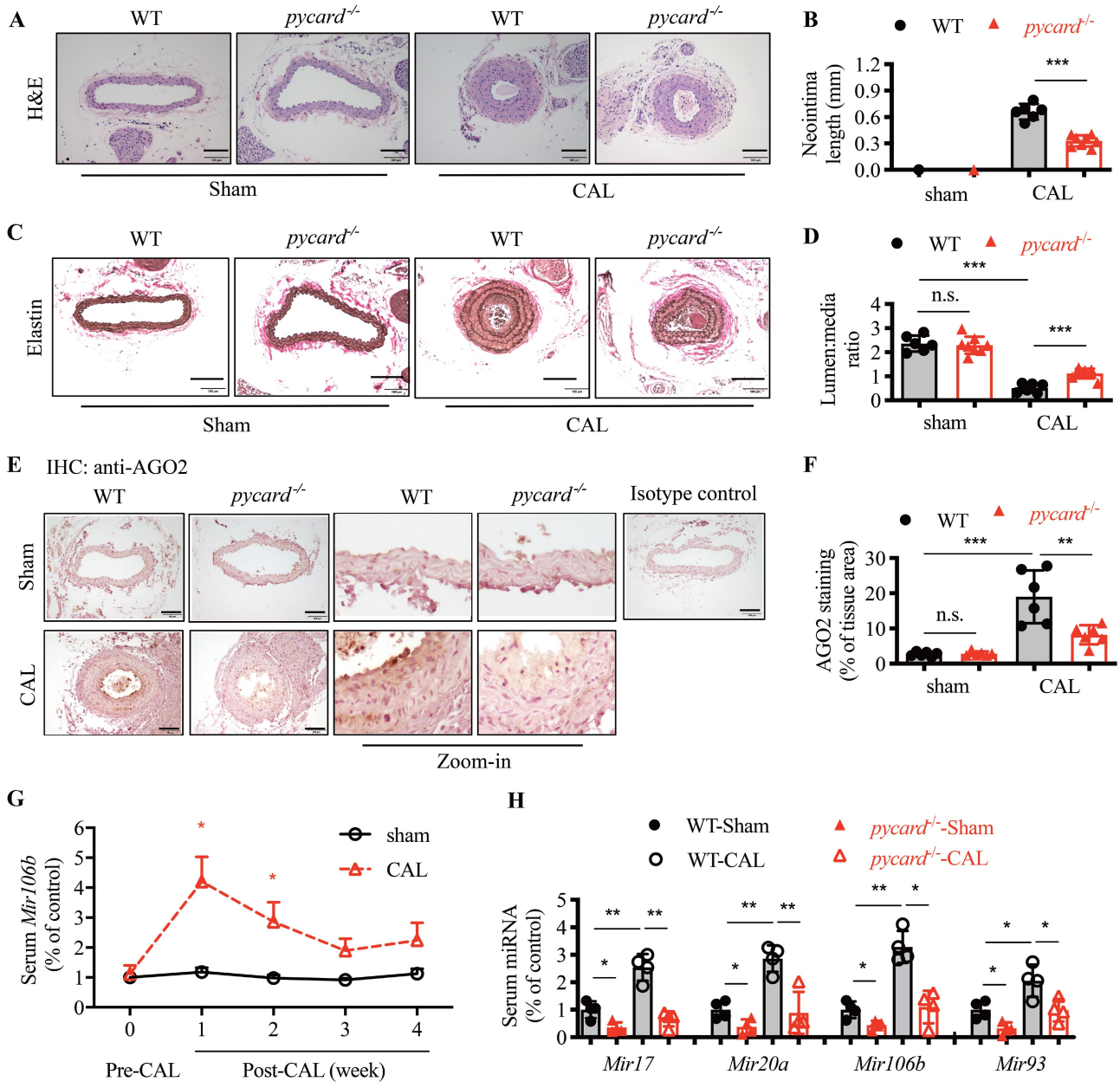

Figure 6. *Pycard*$^{-/-}$ mice exhibits resistance to vascular injury-induced neointima formation. WT and *pycard*$^{-/-}$mice were subjected to sham or carotid artery ligation (CAL) surgery for 28 days. Neointima formation and AGO2 and PRMT8 expression were analyzed. (A) Representative images of H&E staining for carotid artery. Scale bar: 100 µm. (B) quantification of neointima length. (C) Representative images of elastin staining of carotid artery. Scale bar: 100 µm. (D) quantification of relative neointima area (media:lumen ratio). (E) Representative images for AGO2 IHC staining. Scale bar: 100 µm. (F) quantification of IHC staining for AGO2. (G) serum *Mir106b* level was detected at the indicated time points after CAL surgery. (H) serum levels of *Mir17* family members at 1 week after CAL surgery. Data are presented as mean ± SD, $n = 4$–8 mice/group, * $p < 0.05$, ** $p < 0.01$, *** $p < 0.001$, n.S. $p > 0.05$ derived from Student's t tests.

independent roles in controlling some cellular processes [16,17]. In the present study, we have showed for the first time that loss of *Pycard* inhibited adipose tissue-derived miRNA maturation and thus prevented neointima formation in response to vascular injury. Overexpression of AGO2 and administration of *Mir106b* (a major member of *Mir17* family) mimic prevented vascular injury-induced neointima hyperplasia. Mechanistically, *pycard* KO led to asymmetric dimethylarginine modification of AGO2 that controlled miRNA maturation [34] in a PRMT8-dependent manner, which promoted the degradation of AGO2 through CMA pathway (Figure 8).

In addition to storing fat, adipose tissue also produces chemokines, cytokines, and hormones which regulate a variety of physiological processes, including energy balance, immune responses, vascular homeostasis, as well as glucose and lipid metabolism [35]. In the current study, *pycard*$^{-/-}$ mice exhibited a significantly lower level of AGO2, an important enzyme in regulating miRNA biogenesis in EpiAdi, but not in other organs. Lack of *Pycard* did not affect the expression of other proteins related to miRNA biogenesis, including DICER, DROSHA, and DGCR8 in EpiAdi. Consequently, *pycard* KO significantly reduced the mature *Mir17* seed family, including *Mir17-5p*, *Mir20a-5p*,

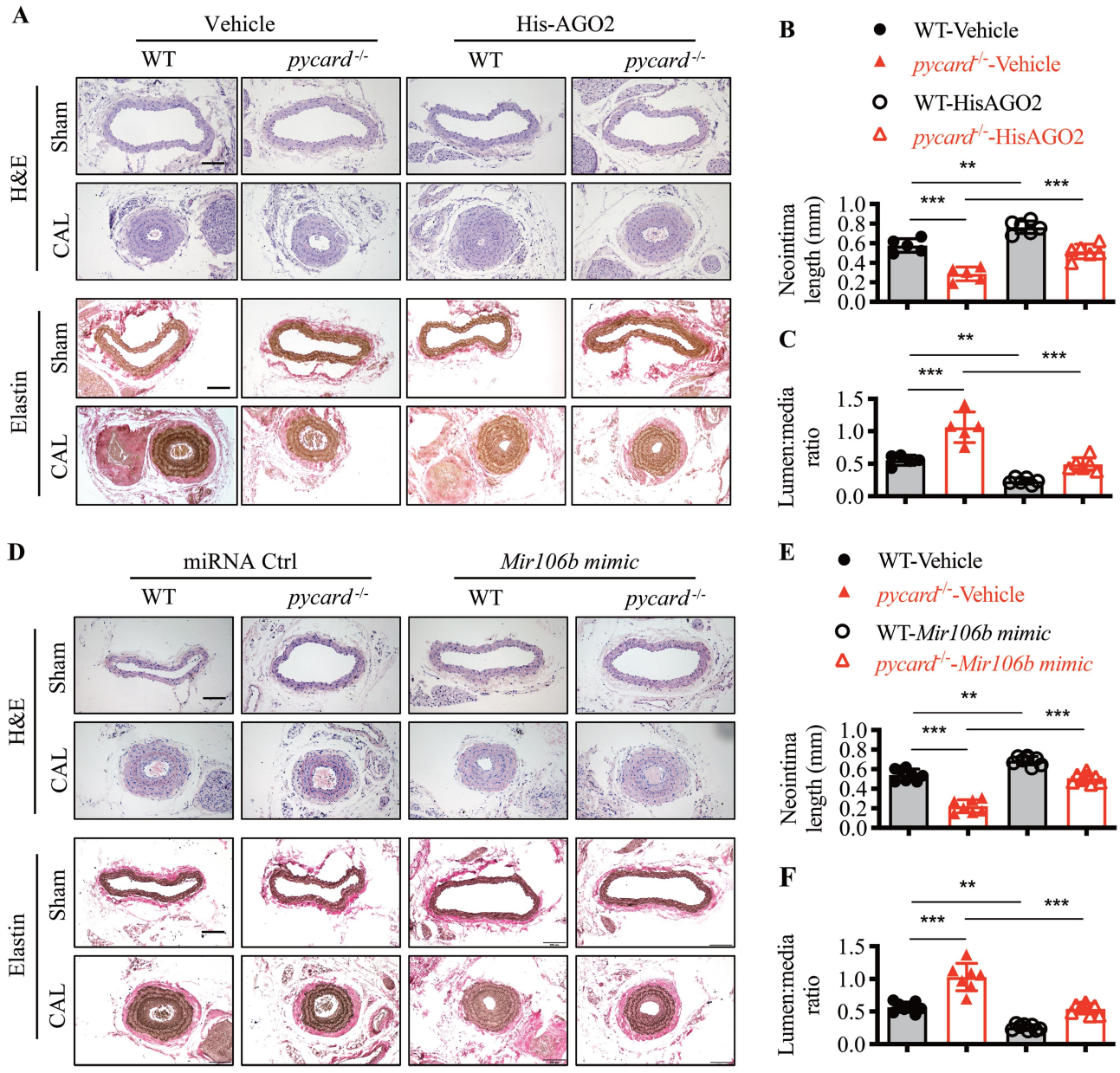

Figure 7. Overexpression of AGO2 and administration of *Mir106b* mimic prevents *pycard* deficiency-mediated inhibition of neointima formation in response to vascular injury. (A-C) left carotid arteries of WT and *pycard*$^{-/-}$ mice were ligated and right carotid arteries were used as sham controls. Both left and right arteries were treated with vehicle or His-tagged AGO2 recombinant protein (His-AGO2) after the surgery. Four weeks after ligation, haemotoxylin and eosin (H&E) and elastin staining were performed on the paraffin sections of carotid arteries to detect neointima formation. Scale bar: 100 µm. (A) Representative images of H&E, and elastin staining of carotid aortas. (B) quantification of neointima length. (C) quantification of relative neointima area (media:lumen ratio). (D-F) left carotid arteries of WT and *pycard*$^{-/-}$ mice were ligated and right carotid arteries were used as sham controls. Both left and right arteries were treated with miRNA control (miRNA Ctrl) or *Mir106b* mimic after the surgery. (D) Representative images of H&E, and elastin staining of carotid artery. Scale bar: 100 µm. (E) quantification of neointima length. (F) quantification of relative neointima area (media:lumen ratio). Data are presented as mean ± SD, $n = 5–8$ mice/group, * $p < 0.05$, ** $p < 0.01$, *** $p < 0.001$, n.S. $p > 0.05$ derived from Student's t tests.

Mir106b-5p, and *Mir93-5p*, but *pycard* KO had no effect on their precursor miRNA expression. These data highlight the importance of adipose tissue in controlling miRNA maturation.

As a common adaptor for a diverse set of inflammasomes, PYCARD has been implicated in many kinds of diseases, including obesity [18,29], vascular diseases [15], and infectious diseases, through inflammasome activation pathways. Furthermore, PYCARD is reported to regulate adaptive immune responses through controlling *Dock2* mRNA stability and expression [18] independently of inflammasome. Our study has identified a novel role of PYCARD in regulating small non-coding RNA biogenesis through regulating CMA-mediated degradation of AGO2. In *pycard*$^{-/-}$ adipocytes AGO2 protein level was significantly lower, suppression of CMA by silencing either *Hspa8* or *Lamp2a* increased AGO2 protein level in WT adipocytes and prevented the reduction of AGO2 protein expression in *pycard*$^{-/-}$ adipocytes. Moreover, *Pycard* deficiency promotes AGO2 binding to CMA effectors (HSPA8 and LAMP2A), promoting the degradation AGO2 through CMA in adipocytes.

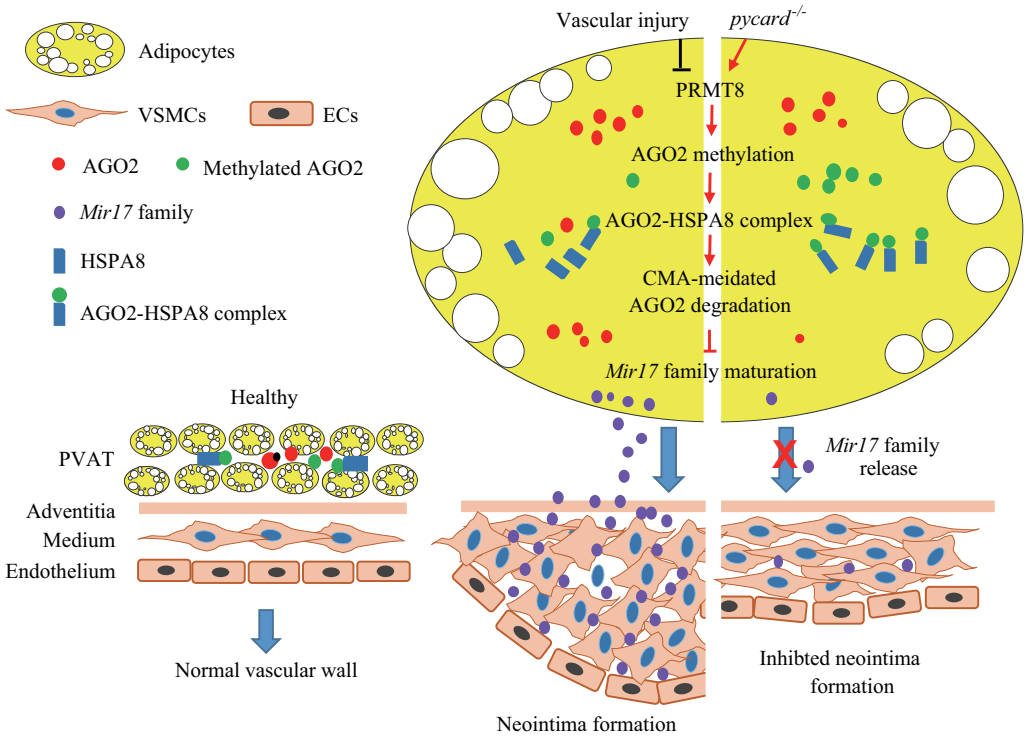

Figure 8. Proposed scheme illustrating the role of *pycard* KO on miRNA maturation and neointima formation. In healthy condition, AGO2 in PVAT regulates miRNA homeostasis, which maintains normal vascular function. *pycard* deficiency increases PRMT8 that induces AGO2 methylation, the methylated AGO2 binds to HSPA8 and increases AGO2 degradation by CMA. The reduction of AGO2 inhibits *Mir106*-family maturation, attenuating vascular injury-induced neointima formation.

AGO2 has been reported to directly interact with HSPA8 [8], and is degraded by CALCOCO2-dependent macroautophagy [7]. However, our observations suggest that CMA is the major mode of autophagy that controls AGO2 degradation in adipocytes, because neither inhibition of proteasome by lactacystin nor suppression of macroautophagy by silencing *Ulk1* influenced AGO2 protein expression, but inhibition of lysosomal degradation with NH_4Cl plus leupeptin and inhibition of lysosomal activity by silencing either *Ctsb* or *Ctsd* significantly increased AGO2 levels. By contrast, activation of CMA by starvation in HBSS or by pharmacological treatment with 6-AN decreased AGO2 levels. In addition, AGO2 could interact with HSPA8 and LAMP2, which are key CMA effectors, and co-localized with lysosomal HSPA8 and LAMP2 in adipose tissue. Disrupting the association between AGO2 and CMA effectors by knockdown of either *Hspa8* or *Lamp2* led to AGO2 protein accumulation.

Our findings also suggest that AGO2 methylation is required for the association betweenAGO2 and HSPA8. We found that lack of *Pycard* increased aDMA modification of AGO2, promoting the association between HSPA8 and AGO2. *Pycard* deficiency significantly enhanced PRMT8 expression. Inhibition of PRMT8 prevented aDAM modification of AGO2, disrupted the association between AGO2 and HSPA8, and reduced CMA-mediated degradation of AGO2. Thus, increased PRMT8-mediated AGO2 methylation interrupts the association between AGO2 and HSPA8 and inhibits CMA-mediated degradation of AGO2 in *Pycard*-deficient conditions.

It is reported that bone marrow-derived PYCARD plays a critical role in neointima formation after vascular injury by regulating the expression of IL1B and IL18 *via* a caspase-1-dependent pathway [15]. In this study, carotid artery ligation surgery dramatically increased the circulating *Mir17* seed family members (including *Mir17*, *Mir106b*, *Mir20a*, and *Mir93*), whereas *pycard* KO suppressed the elevation to maintain the systemic miRNA hemostasis. In agreement with the changes in the *miRNA*, vascular injury-induced neointima formation was prevented in *pycard*$^{-/-}$ mice. Consistently, higher serum levels of *Mir17 ~ 92* cluster members (including *Mir17*, *Mir20a*, *Mir19a*, and *Mir92a*) have been observed in patients with carotid restenosis [31]. Inhibition of *Mir93* suppresses neointima formation after carotid artery injury through targeting MFN2 (mitofusin 2) [36]. *In vivo* administration of antago*Mir92a* significantly reduces neointima formation after balloon injury or arterial stenting through enhancing reendothelialization in injured carotid arteries [37,38]. Conversely, in culture cells *Mir17* stimulates VSMCs proliferation, enhances cell cycle G_1/S transition, and increases proliferating cell nuclear antigen and E2F1 expression [39]. Importantly, application of *Mir106b* mimic aggravated neointima formation in WT mice and prevented the attenuation of vascular remodeling induced by vascular injury in *pycard*$^{-/-}$ mice.

Recent studies have demonstrated that miRNAs are expressed in the vasculature and are involved in human neointima formation. Song, et al, constructed a miRNA-mRNA regulatory work using the data collected from the patients with in-stent restenosis (ISR). In this study, they identified 284 differentially expressed miRNAs and 849 differentially expressed mRNAs in coronary in-stent restenosis [40]. Using microarray analysis of miRNA in plasma from

the patients with ISR, He, et al, found that miRNAs are associated with the occurrence of ISR and can serve as novel noninvasive biomarkers for ISR [41]. In addition, Yuan, et al, analyzed circulating microRNAs expression in 208 participants, including 78 ISR patients, 68 non-ISR patients, and 62 healthy volunteers, using microarray screening. They found that differential circulating miRNA expression in patients after stenting with ISR, indicating that circulating miRNA may have promising value in diagnosing ISR in patients with lower extremity arterial occlusive disease [42]. Although *Mir17* family are not always found in the list of differentially expressed genes in these studies, higher levels of *Mir17* family members have been observed in the serum of patients with carotid restenosis [31]. These studies highlight the importance of miRNAs in diagnosis and treatment of ISR.

There were several limitations in this study. First, IHC staining showed that erythrocytes were also positively stained with AGO2. Although *pycard* KO did not significantly affected AGO2 protein expression in erythrocytes, we cannot not rule out that erythrocyte AGO2 might contribute to increase neointima formation in *Pycard*-deficient conditions, as intralesional erythrocytes was reported to be involved in neointima formation, and erythrocyte AGO2 regulates vascular function in malaria [43,44]. Because we used global *pycard*$^{-/-}$ mice in this experiment, we cannot entirely exclude the possibility that other cells also participate in the regulation of miRNA maturation in *pycard*$^{-/-}$ mice. Thus, using adipocyte-specific *pycard*$^{-/-}$ mice may provide direct evidence to support our hypothesis. Second, we only stained PRMT8 in human femoral tissues because we could not obtain enough specimens to detect the expression PYCARD and AGO2 in human specimens at the same time. In addition, the human specimens used for immunostaining of PRMT8 were from aged donors (around 70–80 years old), whether aging affects PRMT8 expression is still not clear, thus further investigations using specimens from younger and healthy donors are needed to determine the clinic relevance of the PYCARD-PRMT8-AGO2 pathway in neointima formation.

In this study, using mouse CAL model to mimic the clinical in-stent restenosis, we found that ligation of carotid artery enhanced AGO2 expression, while *pycard* KO inhibited AGO2 expression to reduce circulating *Mir106* level, which augmented the protective role of *pycard* KO against vascular remodeling. Recent developments in the understanding of miRNA have suggested their diagnostic and therapeutic potential. Our finding that the PYCARD-AGO2-*Mir17* axis plays a role in carotid artery remodeling suggests that downregulation of *Mir17* family members may serve as a diagnostic biomarker for neointima formation. Overexpression of *Mir106* might be a plausible method to overcome pathological factor-induced neointima hyperplasia.

To conclude, these studies demonstrated that PYCARD controlled CMA-mediated degradation of AGO2, subsequently regulating miRNA maturation, and played a critical role in regulating neointima formation independently of inflammasomes. Our findings identify a previously unknown effect of PYCARD on miRNA maturation in adipose tissue and suggest that modulating PYCARD expression and function may represent a powerful therapeutic strategy for neointima hyperplasia.

Materials and methods

Reagents

Antibodies and reagents are from the following companies: PYCARD (Cell Signaling Technology 67,824; Cell Signaling Technology 13,833), AGO2 (Cell Signaling Technology, 2897; Abcam, ab186733, Santa Cruz Biotechnology, sc -53,521), DICER (Santa Cruz Biotechnology, sc -136,979), DROSHA (Cell Signaling Technology, 3364), DGCR8 (ProteinTech Group 10,996–1-AP), LAMP2 (Abcam, ab125068), HSPA8 (Novus, NB120–2788; Abcam, ab51052), sequestosome1/p62 (Abcam, ab56416), MAP1LC3 (Cell Signaling Technology, 4108), ACTA2/α-SMA (Abcam, ab7817), OPN (Abcam, ab8448), PCNA (ProteinTech Group 10,205–2-AP), CNN/calponin (Cell Signaling Technology 17,819), VIM/vimentin (Cell Signaling Technology, 5741), PRMT8 (Novus, NBP1–55401), SYM10 (Millipore Sigma, 07–412), ASYN24 (Millipore Sigma, 07–414), HSP90 (Cell Signaling Technology, 4874), HSPA/HSP70 (Cell Signaling Technology, 4872), CTSB (Abcam, ab58802), CTSD (Abcam, ab75852), ULK1 (Cell Signaling Technology, 8054), BMP2 (Novus, NBP1–19751), ACTB (Santa Cruz Biotechnology, sc-1616), GAPDH (Santa Cruz Biotechnology 32,233), mouse secondary antibody (Cell Signaling Technology, 7076), rabbit secondary antibody (Cell Signaling Technology, 7074), His-tag (Invitrogen, MA1–21315). *Mir106b-5p* mimic (Life Technologies 4,464,066), mirVana™ miRNA Mimic Negative Control (Life Technologies 4,464,058), mouse AGO2 recombinant protein (Sino Biological 50,683-M07B), human AGO2 recombinant protein (Sino Biological 11,079-H07B). Elastic stain kit (Sigma-Aldrich, HT25A-1KT), Picrosirius Red stain kit (Polysiciences 24,901), mouse AGO2 ELISA Kit (Aviva Systems Biology, OKEH05654), collagenase type I (Worthington, LS004193), pluronic gel (Sigma, P2443), NH_4Cl (Sigma-Aldrich, A9434), leupeptin (Sigma-Aldrich, L2023), 6-AN (Cayman 10,009,315), HBSS (ThermoFisher Scientific 88,284), IBMX (Sigma-Aldrich, I7018), dexamethasone (Sigma-Aldrich, D4902), insulin (Sigma-Aldrich, I6634), anti-dimethyl-arginine antibody, symmetric (SYM10; Millipore Sigma, 07–412) and anti-dimethyl-arginine antibody, asymmetric (ASYM24; Millipore Sigma, 07–414).

Mouse model of CAL injury

Wild-type (WT, C57BL/6J, stock number 000664) and *pycard*$^{-/-}$ mice (stock number 030743) were purchased from The Jackson Laboratories (Bar Harbor, ME, USA). The CAL surgery was performed as described in our previous study [45]. To establish the role of AGO2 in neointima formation, 100 µl of 30% pluronic gel (Sigma, P2443) containing His-AGO2 (1 mg/g) was applied perivascularly to injured carotid arteries immediately after ligation surgery. For perivascular delivery of *Mir106b*, 50 nM of *Mir106b* mimic and miRNA control were packaged in transfection reagent Lipo2000 and dissolved in the autoclaved 30% Pluronic gel. The mixture was applied to the injured arteries immediately after ligation surgery. Four weeks after surgery, carotid arteries were collected for histological analysis. All animal experiments were performed according to protocols approved by the Institutional Animal Care and Use Committee of Georgia State University.

3T3-L1 cells culture

Mouse 3T3-L1 preadipocytes (ATCC, CL-173) were cultured and differentiated into adipocytes using DMEM/F12 (Zen-Bio, DMEMF12-PRF) supplemented with dexamethasone (1 mmol/L), IBMX (0.5 mM), and insulin (1.5 mg/mL, pH 7.4), according to the widely used method [46]. Adipocytes were used 7–10 days after differentiation, when 90–95% of the cells exhibited adipocyte phenotype.

Isolation and culture of mouse primary adipocytes

Primary adipocytes were isolated from the epididymal adipose tissues of male WT or *pycard*$^{-/-}$ mice. Briefly, the adipose tissues were minced into millimeter-sized pieces, and then digested in Krebs-Ringer bicarbonate HEPES (KRBH) buffer (130 mM NaCl, 5 mmol/L $NaHCO_3$, 4.8 mM KCl, 1.2 mM KH_2PO_4, 1 mmol/L $CaCl_2$, 1.2 mM $MgSO_4$, 20 mmol/L HEPES, pH 7.4) with 1% (w:v) bovine serum albumin (Research Products International, A30075–100.0), 1 mg/mL collagenase type I (Worthington, LS004196), 100 μg/mL penicillin, and 100 μg/mL streptomycin for 30 min in a Genie Temp-Shaker 100 at 37°C. The digested samples were filtered through a nylon mesh with pore size 300 μm (pluriSelect, 43 -50,300-50) and centrifuged at 1500 × g for 6 min to separate stromal vascular fraction and adipocytes. Stromal vascular fraction was cultured and differentiated into mature adipocytes as described in 3T3-L1 cells culture.

RNA isolation and quantitative RT-PCR (Q-PCR)

Total RNA was extracted from mouse serum using miRNeasy Serum/Plasma Advanced Kit (Qiagen 217,204) following the manufacturer's instructions. First-strand cDNA was synthesized from mRNA using the All-in-One™ miRNA First-Strand cDNA Synthesis Kit for miRNA qPCR (GeneCopoeia, QP018). Q-PCR was performed using the iQ SYBR Green Supermix (Bio-Rad 1,708,880). The Universal cDNA Synthesis kit (GeneCopoeia, QP017) was used for first-strand synthesis from miRNA. Q-PCR was performed by using miRNA-specific forward and reverse locked nucleic acid (LNA)-enhanced PCR primers from GeneCopoeia. The samples were loaded in duplicate on a CFX Connect TM Real-time PCR detection system. *Actb* and *Rnu6* were used to normalize expression of mRNA and miRNA, respectively. Data were analyzed using the Bio-Rad CFX software. The sequences of the PCR primers are shown in Table S2 and S3.

Microarray analysis of miRNA

Mouse sera were collected from WT and *pycard*$^{-/-}$ mice, and total RNA was extracted from mouse sera using miRNeasy Serum/Plasma Advanced Kit (Qiagen 217,204). MiRNA microarray was performed by Agilent Technologies, Inc [47].

ShRNA, siRNA and miRNA mimic transfections

Stable knockdown of *Ago2* in 3T3-L1 cells was performed using *Ago2* shRNA (Santa Cruz Biotechnology, sc -44,659-V) and control shRNA (Santa Cruz Biotechnology, sc -108,080) according to the manufacturer's instructions.

For transfections of *Cathepsin B* siRNA (Santa Cruz Biotechnology, sc -29,933), *Cathepsin D* siRNA (Santa Cruz Biotechnology, sc -29,934), *Hspa8* siRNA (Santa Cruz Biotechnology, sc -35,593), *Lamp2* siRNA (Santa Cruz Biotechnology, sc -35,791), *Ulk1* siRNA (Santa Cruz Biotechnology, sc -44,849), *Prmt8* siRNA (Santa Cruz Biotechnology, sc -152,473), and *Mir106b* mimic in adipocytes, the cells that had been differentiated for 6 days were electroporated using SE Primary Cell 4D-Nucleofector X Kit (Lonza, V4XC–1012) according to the manufacturer's instructions. 50 nM siRNAs or 100 nM miRNA mimic as well as their correspondent controls were used for transfections. Immediately after electroporation, a volume of 1 ml of cultured medium supplemented with 5 μg/ml insulin was added to the cells. After 24 h of recovery, cells were collected for further analysis.

Immunoprecipitation and immunoblotting analysis

Immunoprecipitation was performed as described previously [48]. Briefly, cells or tissues were collected and lysed in immunoprecipitation lysis buffer (50 mM Tris, 40 mM NaCl, 1 mM EDTA, and 0.5% Triton X-100 [Sigma, T8787], pH 7.4) containing protease inhibitor cocktail (Thermo Scientific 87,786). Protein contents were measured using the Bradford assay (Pierce Biotechnology 23,225). Whole-cell lysates were precleared with protein A agarose beads (GE Healthcare, 17-0780-01) and then subjected to immunoprecipitation with specific antibodies. Generally, 1 μg of antibody was added to 500 μg of cell lysate and incubated overnight at 4°C, and then incubated with protein A agarose beads for 4 h. Immunoprecipitants were washed and eluted with SDS loading buffer by boiling for 5 min and analyzed by immunoblotting. For western blot analysis, lysates were resolved by SDS-PAGE and transferred to polyvinylidene difluoride membrane (Millipore Corp., IPFL00010). Membranes were probed with specific antibodies and subsequently incubated with horseradish peroxidase-linked secondary antibodies. Proteins were visualized by using an enhanced chemiluminescence detection system. The optical densities of the bands were quantified using the AlphaEase (Alpha Innotech Corporation) image system.

Histological, immunochemical and immunofluorescence staining

For morphologic analysis, samples were fixed in 10% formaldehyde and embedded in paraffin as described previously [4]. For carotid artery samples that subjected to CAL surgery, serial 4-μm-thick sections were prepared, covering the range from the ligation site to the area where neointima disappeared. The section number was recorded for neointima length calculation, and sections were stained with H&E and Verhoeff Van Gieson. For IHC staining, deparaffinized sections were stained with indicated antibodies as previously described [19]. The signal was visualized using the Liquid DAB+ Substrate Chromogen System (Dako North America, Inc., K3468), and slides were analyzed with an Olympus microscope. IHC staining density was assessed with a histoscore (HIScore) system described previously [19]. Immunofluorescence staining in cells was carried out according to the method described previously [45,48]. Briefly, 3T3-L1 adipocytes were grown on glass coverslips, fixed with 4%

paraformaldehyde for 30 min, and permeabilized with 0.2% Triton X-100 for 15 min. Adipose tissue sections were permeabilized by incubating in 1% Triton X-100 in phosphate-buffered solution at 25°C for 15 min. After blocking with goat serum, the cells were incubated with AGO2 antibody (1:100 dilution) and HSPA8 antibody (1:300 dilution) or LAMP2 antibody (1:300 dilution), followed by incubation with fluorescein conjugated secondary antibodies. Slides were mounted with Prolong Gold containing DAPI (Invitrogen) and analyzed with an Olympus microscope or LSM 510 Zeiss confocal microscope. Immunofluorescence staining in tissues was performed on frozen sections that were fixed in 4% paraformaldehyde. The sections were blocked with 1% bovine serum and 0.1% Triton X-100 for 2 h at room temperature, and then were treated with primary antibodies. The mouse monoclonal antibody against AGO2 (Santa Cruz Biotechnology, sc -53,521) and rabbit HSPA8 antibody (Abcam, ab51052) were used to determine the colocalization of AGO2 and HSPA8. The mouse monoclonal antibody against AGO2 (Santa Cruz Biotechnology, sc -53,521) and rabbit LAMP2A antibody (Abcam, ab125068) were used to determine the colocalization of AGO2 and LAMP2. The following secondary antibodies were used for immunofluorescence staining: Alexa Fluor 488 goat anti-mouse (Invitrogen 10,337,122), Alexa Fluor 594 goat anti-rabbit (Invitrogen 10,789,623). Images were visualized using a fluorescence microscopy.

Statistical analysis

Data in this study are presented as mean ± S.D. of at least three independent experiments. The comparisons between multiple groups were performed with one-way analysis of variance (ANOVA) followed by a Bonferroni post hoc analysis. The differences between two groups were analyzed by Student's t test. A p value < 0.05 was considered statistically significant.

Acknowledgements

The authors thank Yadong Wang at Center for Inflammation, Immunity and Infection, Institute for Biomedical Sciences, Georgia State University, for her technical assistance, discussions, and valuable insights; thank the help from laboratory technicians, Xicong Tang and Yu Qiu, for their technical assistance.

Disclosure statement

No potential conflict of interest was reported by the authors.

Funding

This study was supported by funding from the following agencies: National Heart, Lung, and Blood Institute (HL089920 and HL142287). Dr. Zou is the Eminent Scholar in Molecular and Translational Medicine of the Georgia Research Alliance.

ORCID

Jian Li http://orcid.org/0000-0003-4517-5819
Hongmin Yao http://orcid.org/0009-0009-6779-5710
Fujie Zhao http://orcid.org/0000-0003-0997-8972
Junqing An http://orcid.org/0000-0003-0091-1501
Qilong Wang http://orcid.org/0000-0002-4375-991X
Zhixue Liu http://orcid.org/0000-0001-7597-5337
Ming-Hui Zou http://orcid.org/0000-0002-3913-0617

References

[1] Bartel DP. MicroRNAs: target recognition and regulatory functions [J]. Cell. 2009;136(2):215–233. doi: 10.1016/j.cell.2009.01.002
[2] Carthew RW, Sontheimer EJ. Origins and mechanisms of miRnas and siRnas. Cell. 2009;136(4):642–655. doi: 10.1016/j.cell.2009.01.035
[3] Davis-Dusenbery BN, Wu C, Hata A, et al. Micromanaging vascular smooth muscle cell differentiation and phenotypic modulation. Arteriosclerosis Thrombosis Vasc Biol. 2011;31(11):2370–2377. doi: 10.1161/ATVBAHA.111.226670
[4] Wang D, Atanasov AG. The microRnas regulating vascular smooth muscle cell proliferation: a minireview. Int J Mol Sci. 2019;20(2):324. doi: 10.3390/ijms20020324
[5] Ha M, Kim VN. Regulation of microRNA biogenesis. Nat Rev Mol Cell Biol. 2014;15(8):509–524. doi: 10.1038/nrm3838
[6] Biasizzo M, Kopitar-Jerala N. Interplay between NLRP3 inflammasome and autophagy. Front Immunol. 2020;11:2470. doi: 10.3389/fimmu.2020.591803
[7] Gibbings D, Mostowy S, Jay F, et al. Selective autophagy degrades DICER and AGO2 and regulates miRNA activity. Nat Cell Biol. 2012;14(12):1314–1321. doi: 10.1038/ncb2611
[8] Tsuboyama K, Tadakuma H, Tomari Y. Conformational activation of argonaute by distinct yet coordinated actions of the Hsp70 and Hsp90 chaperone systems. Molecular Cell. 2018;70(4):722–729. e4. doi: 10.1016/j.molcel.2018.04.010
[9] Gross O, Thomas CJ, Guarda G, et al. The inflammasome: an integrated view. Immunol Rev. 2011;243(1):136–151. doi: 10.1111/j.1600-065X.2011.01046.x
[10] Ren X-S, Tong Y, Ling L, et al. NLRP3 gene deletion attenuates angiotensin II-induced phenotypic transformation of vascular smooth muscle cells and vascular remodeling. Cell Physiol Biochem. 2017;44(6):2269–2280. doi: 10.1159/000486061
[11] Sun H-J, Ren X-S, Xiong X-Q, et al. NLRP3 inflammasome activation contributes to VSMC phenotypic transformation and proliferation in hypertension. Cell Death Dis. 2017;8(10):e3074–e3074. doi: 10.1038/cddis.2017.470
[12] Zhou W, Xi D, Shi Y, et al. MicroRNA-1929-3p participates in murine cytomegalovirus-induced hypertensive vascular remodeling through Ednra/NLRP3 inflammasome activation corrigendum in/10.3892/ijmm. 2022.5082. Int J Mol Med. 2021;47(2):719–731. doi: 10.3892/ijmm.2020.4829
[13] Jin Y, Fu J. Novel insights into the NLRP 3 inflammasome in atherosclerosis. J Am Heart Assoc. 2019;8(12):e012219. doi: 10.1161/JAHA.119.012219
[14] Grebe A, Hoss F, Latz E. NLRP3 inflammasome and the IL-1 pathway in atherosclerosis. Circ Res. 2018;122(12):1722–1740. doi: 10.1161/CIRCRESAHA.118.311362
[15] Yajima N, Takahashi M, Morimoto H, et al. Critical role of bone marrow apoptosis-associated speck-like protein, an inflammasome adaptor molecule, in neointimal formation after vascular injury in mice [J]. Circulation. 2008;117(24):3079–3087. doi: 10.1161/CIRCULATIONAHA.107.746453
[16] Ippagunta SK, Brand DD, Luo J, et al. Inflammasome-independent role of apoptosis-associated speck-like protein containing a CARD (ASC) in T cell priming is critical for collagen-induced arthritis. J Biol Chem. 2010;285(16):12454–12462. doi: 10.1074/jbc.M109.093252
[17] Ellebedy AH, Lupfer C, Ghoneim HE, et al. Inflammasome-independent role of the apoptosis-associated speck-like protein containing CARD (ASC) in the adjuvant effect of MF59. Proc Nat Acad Sci. 2011;108(7):2927–2932. doi: 10.1073/pnas.1012455108
[18] Ippagunta SK, Malireddi RS, Shaw PJ, et al. The inflammasome adaptor ASC regulates the function of adaptive immune cells by controlling Dock2-mediated rac activation and actin

polymerization. Nat Immunol. 2011;12(10):1010–1016. doi: 10.1038/ni.2095
[19] Mercer CA, Kaliappan A, Dennis PB. A novel, human Atg13 binding protein, Atg101, interacts with ULK1 and is essential for macroautophagy. Autophagy. 2009;5(5):649–662. doi: 10.4161/auto.5.5.8249
[20] Kaushik S, Massey AC, Mizushima N, et al. Constitutive activation of chaperone-mediated autophagy in cells with impaired macroautophagy. ?Mol Biol Cell. 2008;19(5):2179–2192. doi: 10.1091/mbc.e07-11-1155
[21] Hao Y, Kacal M, Ouchida AT, et al. Targetome analysis of chaperone-mediated autophagy in cancer cells. Autophagy. 2019;15(9):1558–1571. doi: 10.1080/15548627.2019.1586255
[22] Kirchner P, Bourdenx M, Madrigal-Matute J, et al. Proteome-wide analysis of chaperone-mediated autophagy targeting motifs. PLoS Biol. 2019;17(5):e3000301. doi: 10.1371/journal.pbio.3000301
[23] Chiang H-L, Terlecky SR, Plant CP, et al. A role for a 70-kilodalton heat shock protein in lysosomal degradation of intracellular proteins. Science. 1989;246(4928):382–385. doi: 10.1126/science.2799391
[24] Li L, Fang R, Liu B, et al. Deacetylation of tumor-suppressor MST1 in Hippo pathway induces its degradation through HBXIP-elevated HDAC6 in promotion of breast cancer growth. Oncogene. 2016;35(31):4048–4057. doi: 10.1038/onc.2015.476
[25] Zhang Y, Xu Y-Y, Yao C-B, et al. Acetylation targets HSD17B4 for degradation via the CMA pathway in response to estrone. Autophagy. 2017;13(3):538–553. doi: 10.1080/15548627.2016.1268302
[26] Hu P, Zhao H, Zhu P, et al. Dual regulation of arabidopsis AGO2 by arginine methylation. Nat Commun. 2019;10(1):1–10. doi: 10.1038/s41467-019-08787-w
[27] Scaramuzzino C, Monaghan J, Milioto C, et al. Protein arginine methyltransferase 1 and 8 interact with FUS to modify its sub-cellular distribution and toxicity in vitro and in vivo. PLoS One. 2013;8(4):e61576. doi: 10.1371/journal.pone.0061576
[28] Lee J, Sayegh J, Daniel J, et al. PRMT8, a new membrane-bound tissue-specific member of the protein arginine methyltransferase family. J Biol Chem. 2005;280(38):32890–32896. doi: 10.1074/jbc.M506944200
[29] Stienstra R, Van Diepen JA, Tack CJ, et al. Inflammasome is a central player in the induction of obesity and insulin resistance. Proc Nat Acad Sci. 2011;108(37):15324–15329. doi: 10.1073/pnas.1100255108
[30] Vandanmagsar B, Youm Y-H, Ravussin A, et al. The NLRP3 inflammasome instigates obesity-induced inflammation and insulin resistance. Nature Med. 2011;17(2):179. doi: 10.1038/nm.2279
[31] Luo T, Cui S, Bian C, et al. Crosstalk between TGF-β/Smad3 and BMP/BMPR2 signaling pathways via Mir17–92 cluster in carotid artery restenosis. Mol Cell Biochem. 2014;389(1):169–176. doi: 10.1007/s11010-013-1938-6
[32] Zhang X, Liu J, Wu L, et al. MicroRNAs of the Mir17~ 92 family maintain adipose tissue macrophage homeostasis by sustaining IL-10 expression. Elife. 2020;9:e55676. doi: 10.7554/eLife.55676
[33] Mariathasan S, Newton K, Monack DM, et al. Differential activation of the inflammasome by caspase-1 adaptors ASC and ipaf. Nature. 2004;430(6996):213–218. doi: 10.1038/nature02664
[34] Mallory AC, Elmayan T, Vaucheret H. MicroRNA maturation and action—the expanding roles of ARGONAUTEs. Curr Opin Plant Biol. 2008;11(5):560–566. doi: 10.1016/j.pbi.2008.06.008
[35] Frühbeck G. Overview of adipose tissue and its role in obesity and metabolic disorders. Adipose Tissue Protocols. 2008;456:1–22. doi: 10.1007/978-1-59745-245-8_1
[36] Feng S, Gao L, Zhang D, et al. Mir93 regulates vascular smooth muscle cell proliferation, and neointimal formation through targeting Mfn2. Int J Biol Sci. 2019;15(12):2615. doi: 10.7150/ijbs.36995
[37] Iaconetti C, Polimeni A, Sorrentino S, et al. Inhibition of Mir92a increases endothelial proliferation and migration in vitro as well as reduces neointimal proliferation in vivo after vascular injury. Basic Res Cardiol. 2012;107(5):296. doi: 10.1007/s00395-012-0296-y
[38] Daniel J-M, Penzkofer D, Teske R, et al. Inhibition of Mir92a improves re-endothelialization and prevents neointima formation following vascular injury. Cardiovasc Res. 2014;103(4):564–572. doi: 10.1093/cvr/cvu162
[39] Yang D, Sun C, Zhang J, et al. Proliferation of vascular smooth muscle cells under inflammation is regulated by NF-κB p65/microRNA-17/RB pathway activation. Int J Mol Med. 2018;41(1):43–50. doi: 10.3892/ijmm.2017.3212
[40] Song L, Feng Y, Tian F, et al. Integrated microarray for identifying the hub mRnas and constructed miRNA-mRNA network in coronary in-stent restenosis. Physiol Genomics. 2022;54(10):371–379. doi: 10.1152/physiolgenomics.00089.2021
[41] He M, Gong Y, Shi J, et al. Plasma microRNAs as potential noninvasive biomarkers for in-stent restenosis [J]. PLoS One. 2014;9(11):e112043. doi: 10.1371/journal.pone.0112043
[42] Yuan L, Dong J, Zhu G, et al. Diagnostic value of circulating microRnas for in-stent restenosis in patients with lower extremity arterial occlusive disease. Sci Rep. 2019;9(1):1–7. doi: 10.1038/s41598-018-36295-2
[43] Mantel P-Y, Hjelmqvist D, Walch M, et al. Infected erythrocyte-derived extracellular vesicles alter vascular function via regulatory Ago2-miRNA complexes in malaria [J]. Nat Commun. 2016;7(1):1–15. doi: 10.1038/ncomms12727
[44] Zernecke A, Bidzhekov K, Özüyaman B, et al. CD73/ecto-5′-nucleotidase protects against vascular inflammation and neointima formation. Circulation. 2006;113(17):2120–2127. doi: 10.1161/CIRCULATIONAHA.105.595249
[45] Ouyang C, Li J, Zheng X, et al. Deletion of Ulk1 inhibits neointima formation by enhancing KAT2A/GCN5-mediated acetylation of TUBA/α-tubulin in vivo. Autophagy. 2021;2021(12):1–18. doi: 10.1080/15548627.2021.1911018
[46] An Y, Zhang Y, Li C, et al. Inhibitory effects of flavonoids from abelmoschus manihot flowers on triglyceride accumulation in 3T3-L1 adipocytes. Fitoterapia. 2011;82(4):595–600. doi: 10.1016/j.fitote.2011.01.010
[47] López-Romero P, González MA, Callejas S, et al. Processing of agilent microRNA array data. BMC Res Notes. 2010;3(1):1–6. doi: 10.1186/1756-0500-3-18
[48] Ouyang C, Mu J, Lu Q, et al. Autophagic degradation of KAT2A/GCN5 promotes directional migration of vascular smooth muscle cells by reducing TUBA/α-tubulin acetylation. Autophagy. 2020;16(10):1753–1770. doi: 10.1080/15548627.2019.1707488